Physical properties of the quasi-two-dimensional square lattice antiferromagnet $Ba_2FeSi_2O_7$

Tae-Hwan Jang,[1] Seung-Hwan Do,[1,2] Minseong Lee,[3] Hui Wu,[4] Craig M. Brown,[4] Andrew D. Christianson,[2] Sang-Wook Cheong,[1,5,6] and Jae-Hoon Park[1,7,*]

[1]*MPPHC-CPM, Max Planck POSTECH/Korea Research Initiative, Pohang 37673, Republic of Korea*
[2]*Materials Science and Technology Division, Oak Ridge National Laboratory, Oak Ridge, Tennessee 37831, USA*
[3]*National High Magnetic Field Laboratory (NHMFL), Los Alamos National Laboratory (LANL), Los Alamos, New Mexico 87545, USA*
[4]*NIST Center for Neutron Research, National Institute of Standards and Technology, Gaithersburg, Maryland 20899, USA*
[5]*Laboratory for Pohang Emergent Materials and Department of Physics, Pohang University of Science and Technology, Pohang 37673, Republic of Korea*
[6]*Ruters Center for Emergent Materials and Department of Physics and Astronomy, Rutgers University, Piscataway, New Jersey 08854, USA*
[7]*Department of Physics, Pohang University of Science and Technology, Pohang 37673, Republic of Korea*

(Received 6 September 2021; revised 20 November 2021; accepted 14 December 2021; published 28 December 2021)

We report magnetization (χ, M), magnetic specific heat (C_M), and neutron powder diffraction results on a quasi-two-dimensional (2D) $S = 2$ square lattice antiferromagnet $Ba_2FeSi_2O_7$ consisting of FeO_4 tetrahedrons with highly compressive tetragonal distortion (27%). Despite of the quasi-2D lattice structure, both χ and C_M present three-dimensional magnetic long-range ordering below the Néel temperature $T_N = 5.2$ K. Neutron diffraction data show a collinear $\boldsymbol{Q_m}$ =(1,0,1/2) antiferromagnetic (AFM) structure below T_N but the ordered moment aligned in the *ab* plane is suppressed by 26% from the ionic spin $S = 2$ value ($4\mu_B$). Both the AFM structure and the suppressed moments are well explained by using Monte Carlo simulations with a large single-ion in-plane anisotropy $D = 1.4$ meV and a rather small Heisenberg exchange $J_{intra} = 0.15$ meV in the plane. The characteristic 2D spin fluctuations are recognized in the magnetic entropy release and diffuse scattering above T_N. This new quasi-2D magnetic system also displays unusual nonmonotonic dependence of T_N as a function of magnetic field H.

DOI: 10.1103/PhysRevB.104.214434

I. INTRODUCTION

Two-dimensional (2D) Heisenberg antiferromagnets have been intensively studied both in theory and in experiment to explore exotic low-dimensional magnetic behaviors. The Mermin-Wagner theorem states that no long-range magnetic order can be stabilized at finite temperature in the two-dimensional (2D) Heisenberg magnetic system due to strong spin fluctuations [1]. However, lattice topology and strong magnetic anisotropy are predicted to be able to realize the 2D antiferromagnetic (AFM) ground state [2] as in 2D-Ising and 2D-XY spin systems under an external magnetic field [3–7]. In real layered magnetic materials [8–10], three-dimensional long-range magnetic ordering has often been observed because of the quasi-2D nature with minimal but nonvanishing interlayer magnetic coupling [11,12].

Melilite compounds $A_2MB_2O_7$ (A = Ca, Sr, Ba, M = divalent 3d transition metals, B = Si, Ge) are interesting examples of quasi-2D square lattice Heisenberg AFM systems. The d-p metal-ligand hybridization have been reported to induce various interesting physics such as distinct magnetoelectricity [13], directional dichroism involving spin wave/optical excitations [14], magnetochiral effects [15], and longitudinal magnon modes associated with electromagnons [16,17]. Most studies have been performed on melilite compounds with half-integer spin quantum numbers, M = Mn (5/2), Co (3/2), Cu(1/2) in the last decades. Meanwhile, the studies on the compounds with an integer spin number such as $M = Ni^{2+}$ ($S = 1$) or Fe^{2+} ($S = 2$) have rarely been carried out due to lack of crystals with reliable quality, and thus only a few have been reported recently: a theoretical work on Jahn-Teller distortion driven ferroelectricity in $Ba_2NiGe_2O_7$ [18] and a THz experimental one on spin-orbital excitations in $Sr_2FeSi_2O_7$ [19]. Especially, the Fe ($S = 2$) based compounds present strongly compressed FeO_4 tetrahedrons along the c axis suggesting intriguing magnetic properties governed by a nontrivial magnetic gap [19–22].

A melilite compound $Ba_2FeSi_2O_7$ is crystallized in the $P\bar{4}2_1m$ tetragonal melilite structure as shown in Fig. 1(a) [23]. The lattice constants are $a = 8.3261$ Å and $c = 5.3401$ Å at room temperature. The system is composed of FeO_4 tetrahedra connected via SiO_4 polyhedra, and $FeSi_2O_7$ layers are separated by Ba layers to form a quasi-2D square-lattice structure. The magnetic coupling is dominated by the intralayer Heisenberg interaction (J_{intra}) through the neighboring Fe^{2+}-O^{2-}-O^{2-}-Fe^{2+} exchange path and the layered structure contributes a minimal inter-plane exchange interaction (J_{inter}), resulting in a quasi-2D magnetic system. Noticeably, the FeO_4 tetrahedron is compressed by as large as 27% along the c axis with respect to the perfect tetrahedron. Such a large compression splits both the triplet t_{2g} and doublet e_g orbital states and produce a considerable unquenched orbital angular momentum, which is responsible for

*Corresponding author: jhp@postech.ac.kr

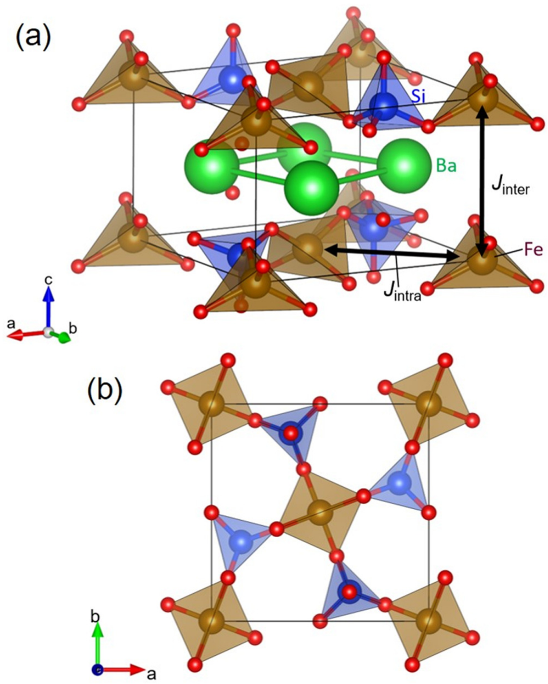

FIG. 1. (a) Crystal structure of $Ba_2FeSi_2O_7$ determined from the neutron diffractions. Thick black arrows indicate the in-plane (J_{intra}) and interplane (J_{inter}) nearest neighbor Heisenberg exchange interactions. (b) A single layer $FeSi_2O_7$ structure. J_{inter} is the exchange interaction between neighboring two Fe^{2+} spins through the Fe^{2+}-O^{2-}-O^{2-}-Fe^{2+} path.

noticeable single-ion anisotropy (D) [20,21]. Considering that $D \sim 1.1$ meV was estimated in $Ba_2CoGe_2O_7$ of 13% compressed CoO_4 tetrahedrons [16,24,25], the D value is certainly enhanced in $Ba_2FeSi_2O_7$ with 27% compression of the FeO_4 tetrahedron.

In this paper, we investigate physical properties of this quasi-2D integer spin ($S = 2$) AFM $Ba_2FeSi_2O_7$ using magnetization, specific heat, and neutron powder diffraction measurements. The results manifest the AFM ordering below the Néel temperature ($T_N = 5.2$ K) with large easy-planar magnetic anisotropy. Using Monte Carlo simulations, we estimate $J_{intra}/D \sim 0.1$. The specific heat measurements reveal a Schottky anomaly arising from thermal populations on low-lying excited spin-orbital states. Neutron diffraction measurements reveal that short-range spin correlations appear below 20 K and that the AFM structure is characterized by a staggered magnetic moment of $2.95\mu_B$, which is considerably (26%) smaller than the moment ($4\mu_B$) expected from $S = 2$. The field dependent measurements exhibit unusual nonmonotonic behavior of $T_N(H)$ as a function of the H field, indicating that the quasi-2D square lattice magnet $Ba_2FeSi_2O_7$ is an easy-planar integer spin system.

II. METHODS

To obtain single crystals of $Ba_2FeSi_2O_7$, we prepared a polycrystalline of $Ba_2FeSi_2O_7$ as a precursor using the solid-state reaction. Stoichiometric mixtures of $BaCO_3$, Fe_2O_3, and SiO_2 were thoroughly ground, pelletized, and heated at 1050 °C with intermediate sintering. X-ray and neutron powder diffraction measurements on the polycrystalline samples identified a dominant phase of $Ba_2FeSi_2O_7$ (96.5%) with minor Ba_2SiO_4 (2.6%) and SiO_2 (0.9%) (see Fig. 6). The polycrystalline samples were prepared as feed rods, and a single crystal of $Ba_2FeSi_2O_7$ was grown using a floating zone melting method under reducing gas atmosphere. The growth direction was perpendicular to the c axis and the size of the as-grown crystal was about 8 mm in diameter and 60 mm in length. The powder XRD pattern on crushed crystals presents a single phase of $Ba_2FeSi_2O_7$, as described in Appendix A.

Temperature (T) and magnetic field (H) dependence of dc magnetization and specific heat measurements on a $Ba_2FeSi_2O_7$ crystal were performed by using a vibrating sample magnetometry (VSM) option and a standard calorimetric relaxation technique equipped in a physical property measurement system (PPMS) of Quantum Design DynaCool-9 T. The magnetization results were compared with classical Monte Carlo simulations in order to estimate the energy scale of the exchange interactions in $Ba_2FeSi_2O_7$. In the simulation, a square lattice of $16 \times 16 \times 6$ spin sites was employed with periodic boundary conditions.

Neutron powder diffraction measurements were carried out using the BT-1 High-Resolution Powder Diffractometer (HRPD) at NIST Center for Neutron Research (NCNR), USA. A 2.9 g polycrystalline sample was loaded into a vanadium can and cooled with a flow-type cryostat. A constant wavelength $\lambda = 2.0772$ Å of the neutron beam was collimated by using a Ge (311)-60° monochromator. Diffraction data were collected at temperatures 1.7, 3, 8, 10, 20, and 30 K. The data refinement was carried out in the Rietveld methods by using the FULLPROF program [26], and the software SARA*h* was used for representational analysis to determine symmetry-allowed magnetic structures [27].

III. EXPERIMENTAL RESULTS

A. Magnetic properties

Figure 2(a) shows temperature dependence of the magnetic susceptibility ($\chi = M/H$) for a $Ba_2FeSi_2O_7$ single crystal with magnetic fields parallel ($H||ab||[110]$) and perpendicular ($H||c||[001]$) to the ab plane. The magnetic susceptibility exhibits strongly anisotropic easy-planar spin behaviors over a broad temperature range. The ab plane is the magnetic easy plane and the c axis is the hard axis. At low temperatures, $\chi(T)$ for both field directions exhibit peaks around $T \sim 8$ K, corresponding to the onset of short-range magnetic order with 2D spin fluctuations. The AFM long-range ordering temperature is determined to be $T_N = 5.2$ K from the sharp peak in the first derivative of the in-plane magnetic susceptibility ($d\chi/dT$).

Inverses of the magnetic susceptibilities in Fig. 2(b) exhibit linear behaviors above 100 K, following the Curie-Weiss formula, $\chi(T) = \chi_0 + C/(T - \Theta_{CW})$ with the Curie constant C, the Curie-Weiss temperature Θ_{CW}, and the diamagnetic contribution χ_0. We determined an effective magnetic moment $\mu_{eff}\,[ab] = 5.56(1)\,\mu_B$, $\mu_{eff}\,[c] = 4.84(1)\,\mu_B$ and Curie-Weiss temperatures $\Theta_{CW}\,[ab] = -7.4(2)$ K, $\Theta_{CW}\,[c] = -23.7(2)$ K from Curie-Weiss fits in the temperature

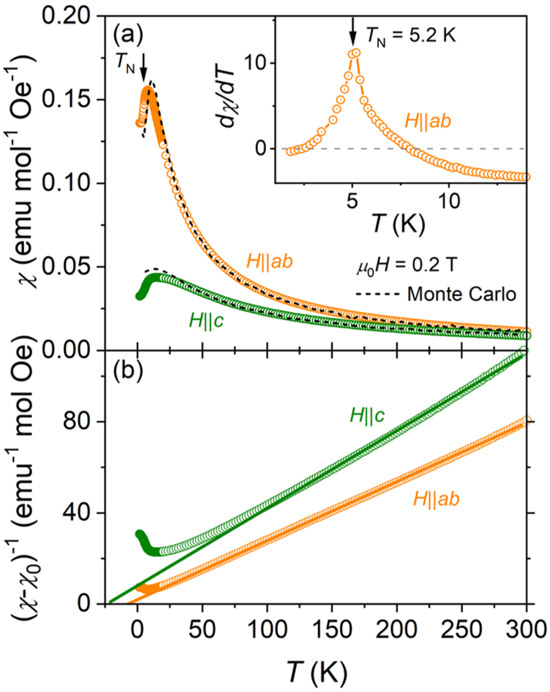

FIG. 2. (a) Temperature (T) dependence of the dc magnetic susceptibility ($\chi = M/H$) with applied magnetic fields $\mu_0 H = 0.2\,\mathrm{T}$ along $H||ab||[110]$ (orange symbol) and $H||c||[001]$ (olive symbol). The dashed lines are the results of classical Monte Carlo simulations with $J_{\mathrm{intra}} = 0.15\,\mathrm{meV}$, $J_{\mathrm{inter}} = 0.0025\,\mathrm{meV}$, $D = 1.4\,\mathrm{meV}$ with a field of 0.2 T. The first derivative of the magnetic susceptibility ($d\chi/dT$) is presented as a function of temperature in the inset. Vertical arrows in (a) denote the magnetic transition at $T_{\mathrm{N}} = 5.2\,\mathrm{K}$. (b) Inverses of the magnetic susceptibilities with magnetic field along $H||ab||[110]$ (orange symbol) and $H||c||[001]$ (olive symbol). Solid lines are Curie-Weiss fits to the data from 100 to 300 K.

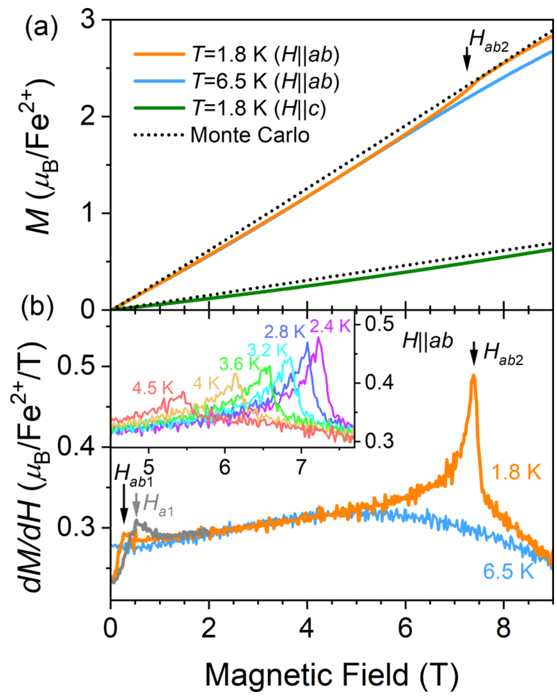

FIG. 3. (a) Magnetic field (H) dependence of magnetization (M) curve along $H||ab||[110]$ (orange and blue symbols for $T = 1.8$ and 6.5 K, respectively) and $H||c||[001]$ (olive symbol, $T = 1.8\,\mathrm{K}$). The dotted lines are the results of classical Monte Carlo simulations with $J_{\mathrm{intra}} = 0.15\,\mathrm{meV}$, $J_{\mathrm{inter}} = 0.0025\,\mathrm{meV}$, and $D = 1.4\,\mathrm{meV}$ (for detailed information about calculation, see Sec. IV). (b) First derivative of magnetization curve (dM/dH) as a function of $H||ab||[110]$ at 1.8 K (orange symbol) and 6.5 K (blue symbol) and of $H||a||[100]$ at 1.8 K (grey symbol, up to 2 T). Vertical arrows indicate positions of critical magnetic fields $\mu_0 H_{ab1} \sim 0.3\,\mathrm{T}$ ($\mu_0 H_{a1} \sim 0.5\,\mathrm{T}$) and $\mu_0 H_{ab2} \sim 7.4\,\mathrm{T}$ showing the H induced weak and sharp peaks in dM/dH at $T = 1.8\,\mathrm{K}$, respectively. The inset in (b) displays dM/dH as a function of $H||ab||[110]$ measured at various temperatures below T_{N}.

range 100–300 K. The out-of-plane moment μ_{eff} [c] is comparable to the spin only value of $S = 2$ ($\mu_{\mathrm{eff}} \sim 4.9\,\mu_{\mathrm{B}}$ for $g = 2$) while the in-plane one μ_{eff} [ab] is considerably larger than the value. It implies that an unquenched angular momentum is present and makes anisotropic contribution to the magnetic moment [21], consistent with the observed anisotropic behavior of χ even up to room temperature. The obtained large Θ_{CW} [c] is attributed to the spin fluctuation involving spin-spin interaction with a strong 2D character.

Figure 3(a) presents isothermal magnetization $M(H)$ as a function of magnetic field H up to 9 T for $H||ab||[110]$ and $H||c||[001]$ at $T = 1.8\,\mathrm{K}$. $M(H)$ shows large anisotropy for $H||ab$ and $H||c$ reflecting the strong easy-planar spin, but both $M_{ab}(H) \equiv M(H||ab)$ and $M_c(H) \equiv M(H||c)$ show linearlike behaviors with H. Interestingly, the slope in $M_{ab}(H)$ changes considerably around $\mu_0 H \sim 0.3\,\mathrm{T}$ ($\mu_0 H_{ab1}$) and $\sim 7.4\,\mathrm{T}$ ($\mu_0 H_{ab2}$). As shown in Fig. 3(b), these anomalies are more noticeable in the derivative dM_{ab}/dH while those disappear at 6.5 K ($>T_{\mathrm{N}}$), indicating that there exist two field-induced transitions below T_{N}. Meanwhile, M_c monotonically increases with H field up to 9 T without any noticeable anomaly representing the field-induced transition. We also observed the weak anomaly around $\mu_0 H_{a1} \sim 0.5\,\mathrm{T}$ in the dM/dH for $H||a||[100]$ at $T = 1.8\,\mathrm{K}$ [Fig. 3(b)]. As the magnetic field is applied away from the easy axis, the Zeeman energy cost is required to increase the critical field for the transition. Thus, the slightly smaller value of $\mu_0 H_{ab1}$ than one of $\mu_0 H_{a1}$ implies that the easy axes are likely along [110] and [1–10] directions in the ab plane. We note that the dM/dH for both $H||a||[100]$ and $H||b||[010]$ shows almost the same H dependence and the critical magnetic fields (not shown here), indicating that the fourfold in-plane anisotropy exists by the crystallographic symmetry. The calculated in-plane magnetic anisotropy energy is about 0.05 meV.

The low field transition at H_{ab1} can be attributed to a spin-flop-like transition aligning two AFM domains. At the $H = 0$ field (AFM-I phase), there exist two equally populated AFM domains: the AFM ordered spins along in-plane easy axis [110] in one and [1–10] in the other. At H increases across H_{ab1}, the spin axes of both domains align to be perpendicular to the H direction in the ab plane (AFM-II phase). A similar transition was also observed in $Ba_2CoGe_2O_7$ [25]. H_{ab1} exhibits almost no temperature dependence below T_{N} (not shown here) and disappears above T_{N}. On the other hand, the high field transition enhances M_{ab} across H_{ab2}, and the

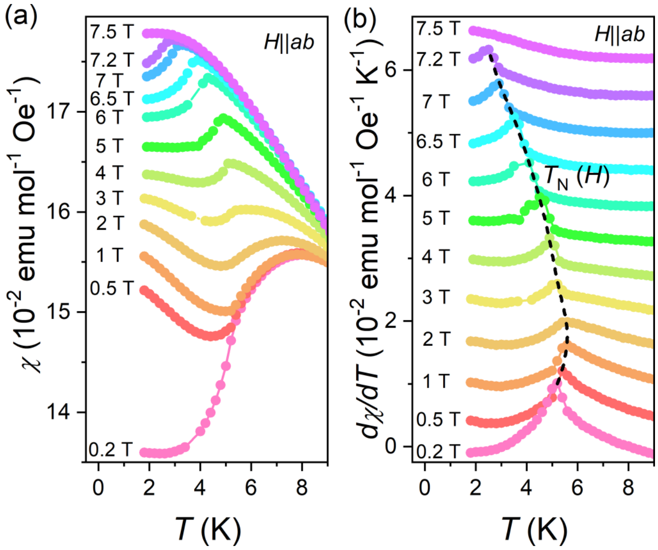

FIG. 4. (a) Temperature (T) dependence of the dc magnetic susceptibility ($\chi = M/H$) and (b) first derivatives of magnetic susceptibility ($d\chi/dT$) as a function of T for applied magnetic fields along $H||ab||[110]$. In (b), the dotted guide line indicates $T_N(H)$ determined from the peak positions in $d\chi/dT$. For clarity, each $d\chi/dT$ curve is vertically shifted by 0.006 emu mol^{-1} Oe^{-1} K^{-1}.

enhanced magnetic moment $\Delta M_{ab}(T) = M_{ab}(T)$–$M_{ab}(6.5\text{ K})$ is estimated to be $\sim 0.15\,\mu_B/Fe^{2+}$ at $T = 1.8$ K. To trace the anomalies, we measured $M_{ab}(H)$ at different temperatures below T_N. The inset shows dM_{ab}/dH as a function of H at various temperatures below T_N. As temperature increases, the dM/dH peak feature becomes weaker and H_{ab2} shifts to low fields. The peak disappears above T_N, indicating that this transition is also relevant to the AFM order.

Figure 4(a) shows $\chi(T)$ as a function of temperature T measured at various $H||ab||[110]$ fields up to $\mu_0 H = 7.5$ T. $\chi(T)$ below T_N suddenly changes between 0.2 and 0.5 T due to the spin-flop-like transition across $\mu_0 H_{ab1} \sim 0.3$ T [Fig. 3(b)]. As presented in Fig. 4(b), the derivatives $d\chi/dT$ clearly exhibit peak features representing the AFM transition up to $\mu_0 H = 7.2$ T ($<\mu_0 H_{ab2}$) and enable us to determine $T_N(H)$ at a given $H||ab$ field. Interestingly, $T_N(H)$ shows a nonmonotonic field dependent behavior. $T_N(H)$ slightly increases as H increases up to $\mu_0 H \sim 2$ T, and then it decreases for further increasing H up to 7.2 T. At $\mu_0 H = 7.5$ T ($>\mu_0 H_{ab2}$), the $d\chi/dT$ peak feature becomes completely suppressed with saturation in $\chi(T)$.

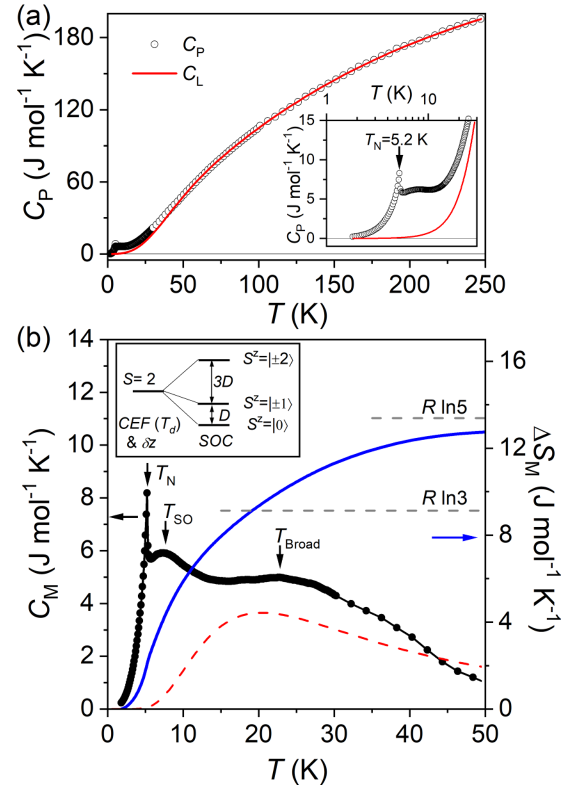

FIG. 5. (a) Total specific heat (C_P). Open circles and a red line display the measured total specific heat (C_P) and the calculated lattice contribution of specific heat (C_L), respectively. Inset displays the magnified C_P and C_L below 30 K in a semilogarithmic scale. The vertical arrow indicates the magnetic transition temperature ($T_N = 5.2$ K). (b) Magnetic specific heat (left panel: $C_M = C_P - C_L$, black symbols) and magnetic entropy gain (right panel: ΔS_M, blue line) as a function of temperature. Above T_N, C_M shows two broad peaks centered at $T_{SO} \sim 8$ K and $T_{Broad} \sim 23$ K, associated with short-range spin correlations and a Schottky anomaly from the excitations between the spin S^z states, respectively. Two gray horizontal dashed lines show $R\ln(2S+1)$ for $S = 1$ ($R\ln 3$) and $S = 2$ ($R\ln 5$). Inset represents the energy level structure of the lowest d_{z^2} orbital for the Fe^{2+} ion in the tetrahedral crystal field (T_d) with a tetragonal compression (δz) and energy levels of the S^z states further split by the spin-orbit coupling (SOC) [19,20]. A red dashed curve indicates the calculated Schottky anomaly for the transition between $S^z = |\pm 2\rangle$ and $S^z = |\pm 1\rangle$ states with gap, $\Delta = 3D = 3 \times 1.4\,\text{meV} = 4.2\,\text{meV}$ where D is referred to the Monte Carlo calculations (see the text).

B. Specific heat

Figure 5(a) shows total specific heat (C_P) of $Ba_2FeSi_2O_7$ at $H = 0$. Lattice contribution (C_L) was estimated from the Debye-Einstein model, where $C_L(T)$ is defined as [28,29]

$$C_L(T) = m\left[9Rx_D^{-3}\int_0^{x_D}\frac{x^4e^x}{(e^x-1)^2}\right] + \sum_{i=1}^{s-1} n_i\left[3R\frac{x_{E_i}^2 e^{x_{E_i}}}{(e^{x_{E_i}}-1)^2}\right]. \quad (1)$$

The first term represents the Debye specific heat for the acoustic phonon modes and the second term represents the Einstein specific heat for optical phonon modes. x_D and x_{Ei} are defined as $x_D = \Theta_D/T$ and $x_{Ei} = \Theta_{Ei}/T$ where Θ_D and Θ_{Ei} are the Debye temperature and the Einstein temperatures, respectively. The constants m and n_i are the number of degrees of freedom for each contribution and R is the molar gas constant. Fitting Eq. (1) to the experimental data in a range 70–250 K provides $\Theta_D \sim 237$ K ($m = 4.8$), $\Theta_{E1} \sim 554$ K ($n_1 = 4.3$), and $\Theta_{E2} \sim 1345$ K ($n_2 = 2.9$) with $m + n_1 + n_2 = 12$ (total number of atoms in the formula unit). Based on these fitting parameters, the extracted C_L is displayed in Fig. 5(a). Magnetic specific heat (C_M) shown in Fig. 5(b) was obtained by subtracting the lattice contribution from the total specific heat, i.e., $C_M = C_P - C_L$. C_M displays a sharp λ anomaly at $T_N = 5.2$ K, which coincides with T_N determined from the magnetic susceptibility. Above T_N, C_M exhibits a broad peak around $T_{SO} \sim 8$ K, which represents the short-range ordering with suppression of the long-range order due to the low dimensionality [2].

The magnetic entropy $\Delta S_M(T)$ was calculated by using $\Delta S_M(T) = \int_0^T \Delta C_M(T)/T dT$. ΔS_M at $T = 50$ K is obtained to be 12.74 J mol^{-1} K^{-1} that corresponds to 95% of $R\ln(2S+1) = R\ln5$, the total entropy of $S = 2$. We note that only about 20% of the total entropy is released at T_N and additional entropy involving the short-range order is released by above the transition temperature ($T_{SO} \sim 8$ K). Interestingly, the entropy $R\ln(3) \sim 9.13$ J mol^{-1} K^{-1} corresponding to the degree of freedom for $S = 1$ effectively releases up to around 18 K, where the short-range ordering peak diminishes. Above this temperature, a Schottky-like broad peak is visible in C_M around $T_{Broad} \sim 23$ K and the entropy gradually releases the remnant of the $S = 2$ spin degree of freedom up to even above 50 K.

C. Powder neutron diffraction

To study the AFM spin structure below T_N, we have carried out zero field ($H = 0$) neutron powder diffraction (NPD) measurements on $Ba_2FeSi_2O_7$. Figure 6 shows the NPD patterns at 30 K ($>T_N$) and 1.7 K ($<T_N$). The crystal and magnetic structures were determined from the Rietveld refinement fitting by using FULLPROF [26]. The refined crystallographic parameters are tabulated in Table I ($T = 30$ K) and Table II ($T = 1.7$ K). Both the $T = 30$ K and $T = 1.7$ K diffraction patterns for the nuclear Bragg peaks are well described by the tetragonal space group $P\bar{4}2_1m$ (SG: 113), and the Bragg peak profiles exhibit only small variations across T_N, evidencing that the AFM transition does not accompany any considerable structural transition. Comparing the low-Q region (0.5 Å$^{-1} \leqslant Q \leqslant 2.0$ Å^{-1}) diffraction patterns at $T = 1.7$ and 30 K as shown in the inset, we identify the magnetic Bragg reflections at $\boldsymbol{Q} = (1,0,1/2)$ and (2,1,1/2) below T_N, indicating the characteristic vector of $\boldsymbol{Q_m} = (1,0,1/2)$.

Representation analyses were used to determine symmetry-allowed magnetic structures. Irreducible representations $\Gamma_{mag} = 1\Gamma^1{}_1 + 1\Gamma^1{}_2 + 2\Gamma^2{}_5$ are compatible with the $P\bar{4}2_1m$ symmetry with two Fe sites at (0,0,0) and (1/2,1/2,0). The basis vectors of $2\Gamma^2{}_5$ reproduce all of magnetic Bragg peaks with a collinear antiferromagnetic spin structure as depicted in Figs. 7(a) and 7(b). The in-plane collinear AFM spin alignment indicates that the nearest neighbor spin-spin interaction is governed by the Heisenberg J_{intra} through the in-plane Fe^{2+}-O^{2-}-O^{2-}-Fe^{2+} exchange path (see Fig. 1). The ordered magnetic moment is determined to be 2.95μ_B, which is only 74% of the full moment of Fe^{2+} spin ($S = 2$).

Figure 7(c) shows evolution of the magnetic peak intensity at $\boldsymbol{Q_m} = (1,0,1/2)$ ($Q = 0.95$ Å^{-1}) with temperature. Figure 7(d) presents NPD measured at different temperatures from 3 to 30 K. The sharp and intense magnetic Bragg peak, which is present at $Q = Q_m = 0.95$ Å^{-1} in the 3 K scan, mostly diminishes at 8 K. A small peak at $Q_m = (1,0,1/2) \sim 0.95$ Å^{-1} in the 8 K data is likely due to the significant 3D short-range correlations at $T_N < T \sim T_{SO}$. Note that the small peak near $Q = 0.95$ Å^{-1} remaining at 20 and 30 K is most likely a small impurity peak (Appendix B). Besides minimal remnant of the sharp magnetic peak, an additional broad peak feature is observable around $Q = 0.8$ Å^{-1} (marked with a black arrow) in the 8 K scan. The broad peak around $Q = (1,0,0) \sim 0.75$ Å^{-1} (close to 0.8 Å^{-1}) is from the 2D correlations with magnetic form factor distribution and is observed in 20 K. This feature gradually fades out and shifts to low Q upon heating, and then finally disappears at 30 K, well above

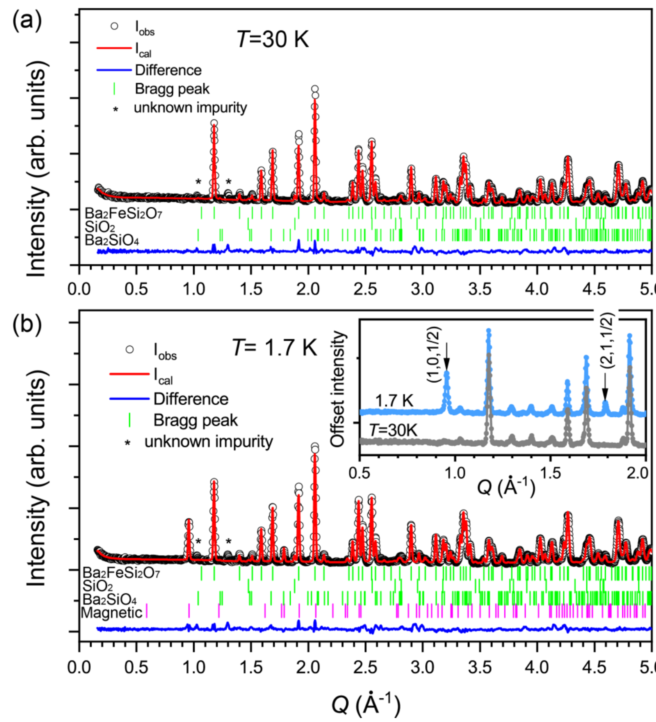

FIG. 6. Neutron powder diffraction patterns for $Ba_2FeSi_2O_7$ at (a) $T = 30$ K ($>T_N$) and (b) 1.7 K ($<T_N$). Open circles and a red solid line represent the experimental data and the Rietveld refinement fitting line, respectively. At both temperatures, Bragg peaks from SiO_2 and Ba_2SiO_4 (nonmagnetic secondary phases) are visible in the sample, and the Rietveld refinement quantifies the phase fractions of 0.9% and 2.6%, respectively. In (b), the structural and magnetic Bragg reflections are presented by upper (green) and low (violet) ticks, respectively. The inset shows an expanded view of the low-Q region data and miller indexed magnetic peaks indicated by arrows. Asterisk marks at two peaks are from an unknown impurity phase.

TABLE I. Crystallographic parameters with space group $P\bar{4}2_1m$ (SG:113) from Rietveld refinements on the diffraction data at $T = 30$ K. Lattice constants $a = b = 8.3193(8)$ Å, $c = 5.3348(5)$ Å, and $\alpha = \beta = \gamma = 90^\circ$. $R_{wp} = 6.75\%$.

Atom	Site	x	y	z	B
Ba	$4e$	0.1648(3)	0.6648(3)	0.5090(6)	0.05(12)
Fe	$2a$	0	0	0	0.05(4)
Si	$4e$	0.3627(3)	0.8627(3)	0.9610(7)	0.12(12)
O1	$2c$	0	0.5	0.1371(8)	0.36(8)
O2	$8f$	0.3649(3)	0.8649(3)	0.2627(5)	0.17(6)
O3	$4e$	0.0764(3)	0.1990(2)	0.1712(4)	0.15(5)

TABLE II. Crystallographic parameters with space group $P\bar{4}2_1m$ (SG:113) from Rietveld refinements on the diffraction data at $T = 1.7$ K. Lattice constants $a = b = 8.3194(2)$ Å, $c = 5.3336(5)$ Å, and $\alpha = \beta = \gamma = 90^\circ$. $R_{wp} = 7.14\%$.

Atom	Site	x	y	z	B
Ba	4e	0.1644(3)	0.6644(3)	0.5098(7)	0.08(10)
Fe	2a	0	0	0	0.20(5)
Si	4e	0.3645(3)	0.8645(3)	0.9609(7)	0.11(8)
O1	2c	0	0.5	0.1383(8)	0.54(9)
O2	8f	0.3651(3)	0.8651(2)	0.2642(5)	0.07(6)
O3	4e	0.0769(3)	0.1984(2)	0.1694(5)	0.32(5)

T_N. This Q-dependent diffusive scattering is attributed to short range spin-spin correlations, which were also observed in the magnetic specific heat $C_M(T)$ as a broad peak feature around $T_{SO} \sim 8$ K (see Fig. 5). The presence of the diffusive scattering feature reflects strong spin fluctuations in the low dimensional quasi-2D magnetic system.

IV. DISCUSSION

We observe multiple magnetic transitions with temperature and in-plane magnetic fields ($H||ab||[110]$) in the magnetization and specific heat measurements. Those transitions can be summarized with a phase diagram in an H-T space as shown in Fig. 8. The phase boundaries are defined by the peak positions determined from $d\chi/dT$, dM/dH, and C_M. At a zero field, the system is in the AFM-I phase with two types of AFM domains below T_N, and transits to the paramagnetic phase (PM) upon heating across T_N. On the other hand, as H increases across $\mu_0 H_{ab1} \sim 0.3$ T well below T_N, the AFM-I phase transits to the AFM-II phase with a single type of AFM domain. The AFM ordered spins, which lie to be nearly perpendicular to the H direction, slightly cant toward the H direction and result in a finite M, i.e., a composition of AFM and ferromagnetic (FM) components (field induced canted AFM). As the H field further increases, the AFM component decreases and finally disappears. The AFM-II phase transits to the spin polarized (SP) phase across H_{ab2} with a certain gain of ΔM. $\mu_0 H_{ab2} \sim 7.4$ T determined from $M(H, T)$ at 1.8 K decreases as T increases (see Fig. 3). $H_{ab2}(T)$ nearly coincides with $T_N(H)$ from $\chi(H, T)$ (see Fig. 4) up to $T \sim 4$ K. Upon further heating, $H_{ab2}(T)$ somewhat deviates from $T_N(H)$ and finally disappears at $T > \sim 5$ K (or $\mu_0 H < \sim 4$ T), implying that the SP phase crosses over to the PM phase.

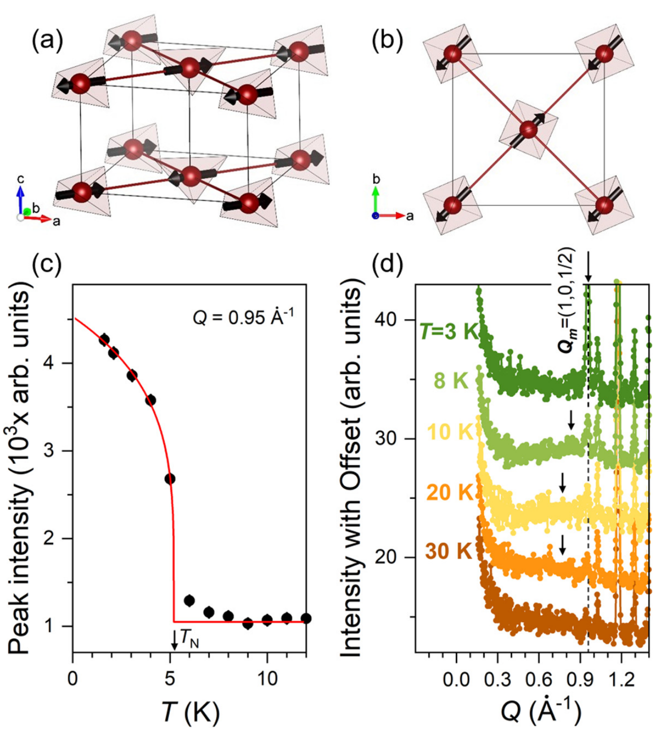

FIG. 7. (a),(b) Magnetic structure of $Ba_2FeSi_2O_7$. The structure is a collinear spin alignment of Fe spins with $\boldsymbol{Q}_m = (1,0,1/2)$ ($= 0.95$ Å^{-1}). (c) Magnetic peak intensity at $Q = 0.95$ Å^{-1} as a function of temperature (black closed circles). The red solid line is a guide to eye, and $T_N = 5.2$ K is indicated by a vertical arrow. Near constant intensity above T_N reflects the structural contribution at Q. (d) Neutron powder diffraction patterns at different temperatures as indicated in the figure.

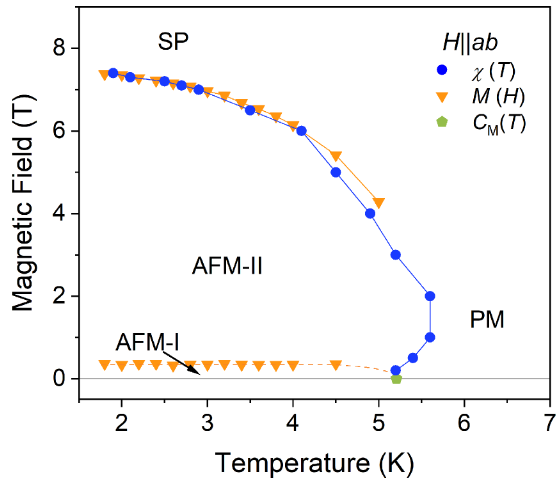

FIG. 8. Magnetic phase diagram of the $Ba_2FeSi_2O_7$ with applied magnetic field $H||ab||[110]$. Blue and green symbols present T_N determined from the magnetic susceptibility and specific heat measurements, respectively. Orange symbols represent critical magnetic fields (H_{ab1}, H_{ab2}) determined from the magnetization measurements. AFM-I, AFM-II, SP, and PM denote antiferromagnetic (two types of AFM domains), field induced canted antiferromagnetic, spin-polarized, and paramagnetic phases, respectively.

We note that $T_N = 5.2$ K at $H = 0$ increases up to 2 T and then decreases above 2 T as H increases. This nonmonotonic behavior of $T_N(H)$ was also observed in other quasi-2D spin systems with a very weak interlayer exchange coupling (J_{inter}) [9,10]. At a low magnetic field, the S^z spin fluctuation becomes suppressed and the spin correlation within the ab plane becomes effectively enhanced to increase T_N. At a high field, the spin canting effect prevails to reduce T_N as usual. Appearance of the nonmonotonic behavior of $T_N(H)$ manifests that $Ba_2FeSi_2O_7$ is a spin system with the strong 2D character. It is also consistent with remarkable short-range spin correlation above T_N observed in specific heat and neutron diffraction results.

To quantify energy scales of the exchange interactions and single-ion anisotropy, we performed Monte Carlo simulations to calculate the magnetic properties. The calculated $\chi(T)$ and $M(H)$ are compared with the corresponding experimental ones in Figs. 2 and 3, respectively. For the simulation, we constructed a simple spin Hamiltonian only consisting of Heisenberg exchange interactions, a single-ion anisotropy, and a Zeeman term for $S = 2$ as follows:

$$H = J_{\text{intra}} \sum_{\langle i,j\rangle_1} \mathbf{S}_i \cdot \mathbf{S}_j + J_{\text{inter}} \sum_{\langle i,j\rangle_2} \mathbf{S}_i \cdot \mathbf{S}_j + D \sum_i \left(S_i^z\right)^2 - \mu_B \sum_i \mathbf{S}_i \cdot \mathbf{g} \cdot \mathbf{B},$$

where $\langle i, j\rangle_1$ and $\langle i, j\rangle_2$ denote the in-plane and interplane nearest neighbors, respectively. The direction of z is parallel to the c axis [see Fig. 1(a)]. Although it is not possible to uniquely determine values of the exchange parameters, we could quantify $J_{\text{intra}} = 0.15$ meV, $J_{\text{inter}} = J_{\text{intra}}/60$, and $D = 1.4$ meV, $g_{ab} = 2.6$, and $g_c = 2.3$, which fairly well reproduce T_N, high temperature $\chi(T)$ above 50 K [Fig. 2(a)], and the magnetic anisotropy $M(H)$ [Fig. 3(a)]. $\chi(T)$ below 50 K deviates from the Curie-Weiss formula. We ascribe this deviation to thermal depopulations of the high energy spin states split by the strong single-ion anisotropy, which are not taken into in our classical Monte Carlo simulations.

Together with tetragonal compression of FeO_4 tetrahedrons along the z direction in $Ba_2FeSi_2O_7$, the spin-orbit coupling (SOC) splits the $S = 2$ state with $(2S + 1)$-fold degeneracy into one singlet ground state ($S^z = 0$) and two doublet excited states ($S^z = |\pm 1\rangle$ and $S^z = |\pm 2\rangle$) with finite gaps of D and $3D$, respectively [see inset in Fig. 5(b)] [19–21]. Hence these low-lying ground/excited spin states are governed by thermal populations in the temperature range of $4D$ (5.6 meV ~ 70 K) energy scale. The residual broad peak around 23 K in C_M is considered to be associated with the thermal populations of $S^z = |\pm 1\rangle$ and $S^z = |\pm 2\rangle$ states. The Schottky anomaly for the gap $\Delta = 3D$ with $D = 1.4$ meV from the Monte Carlo simulation [red dashed line in Fig. 5(b)] reproduces the peak position and width of the observed broad peak. This D value agrees with the value obtained from the recent inelastic neutron scattering study [22]. The thermal populations of the excited states ($S^z = |\pm 1\rangle$ and $S^z = |\pm 2\rangle$) were also similarly observed in the THz absorption data of a sister compound $Sr_2FeSi_2O_7$ (denoted by β-mode absorption) [19]. It is worthwhile to note that magnetic susceptibility along the c axis deviates from the Curie-Weiss formula below 70 K, which is consistent with the onset temperature of the Schottky anomaly peak. The deviations in χ_c and the Schottky peak evidence the presence of a single-ion anisotropy in $Ba_2FeSi_2O_7$.

V. CONCLUSION

In summary, we have studied the effects of the large single-ion anisotropy (D) on the physical properties in the new $S = 2$ quasi-2D square lattice antiferromagnet $Ba_2FeSi_2O_7$ with M, χ, C_M, and NPD measurements. The gapped spin states and their thermal populations are responsible for the remarkable 2D spin fluctuation behaviors such as Schottky anomaly and short-range magnetic ordering with strong release of the magnetic entropy gain. On the other hand, below $T_N = 5.2$ K, M and χ exhibit large easy-planar magnetic anisotropy, and the NPD data yield a significantly reduced magnetic ordered moment. As the easy-planar anisotropy gap energy D increases, the system with an integer S could favor a quantum disordered paramagnetic ground state (local $S^z = 0$) rather than the AFM one [30,31]. We suspect that the AFM $Ba_2FeSi_2O_7$ may be near the quantum critical point of these two competing magnetic states. In this case, Higgs modes like the longitudinal magnon modes are possibly observable in the low-energy spin excitation spectra of the inelastic neutron scattering or Raman spectroscopy [22,32–34]. The presented magnetic results and the constructed magnetic phase diagram suggest that $Ba_2FeSi_2O_7$ is an important example of the $S = 2$ quasi-2D square lattice Heisenberg antiferromagnet with a

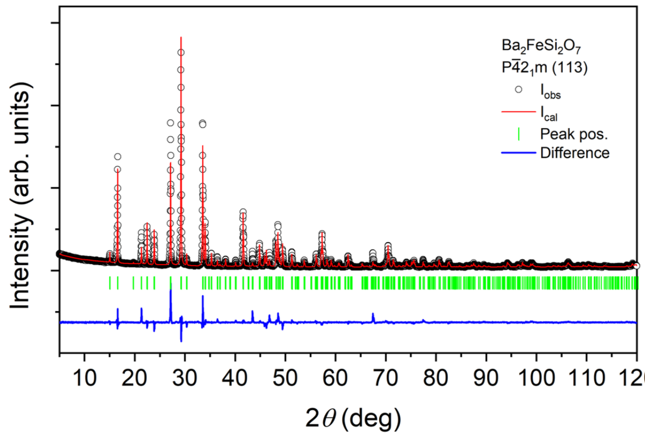

FIG. 9. X-ray diffraction (XRD) pattern from crushed single crystals of $Ba_2FeSi_2O_7$ collected at $T = 300$ K. Open circles represent experimental data and solid line in red indicates a fitted line from Rietveld refinement using FULLPROF [26]. The blue solid line indicates the difference between experimental data and the fitted line. Green tick marker indicates the location of Bragg reflections for $Ba_2FeSi_2O_7$ phase.

TABLE III. Crystallographic parameters with space group $P\bar{4}2_1m$ (SG:113) from Rietveld refinements on the diffraction data at $T = 300$ K. Lattice constants $a = b = 8.3261(2)$ Å, $c = 5.3402(1)$ Å, and $\alpha = \beta = \gamma = 90^\circ$. $R_{wp} = 20.2\%$.

Atom	Site	x	y	z	B
Ba	4e	0.1693(1)	0.6693(1)	0.5098(4)	1.33(2)
Fe	2a	0	0	0	0.60(9)
Si	4e	0.3689(5)	0.8689(5)	0.9665(13)	1.17(16)
O1	2c	0	0.5	0.1182(30)	0.35(44)
O2	8f	0.3452(15)	0.8452(15)	0.2767(19)	1.85(34)
O3	4e	0.0738(12)	0.1996(11)	0.1722(11)	0.51(22)

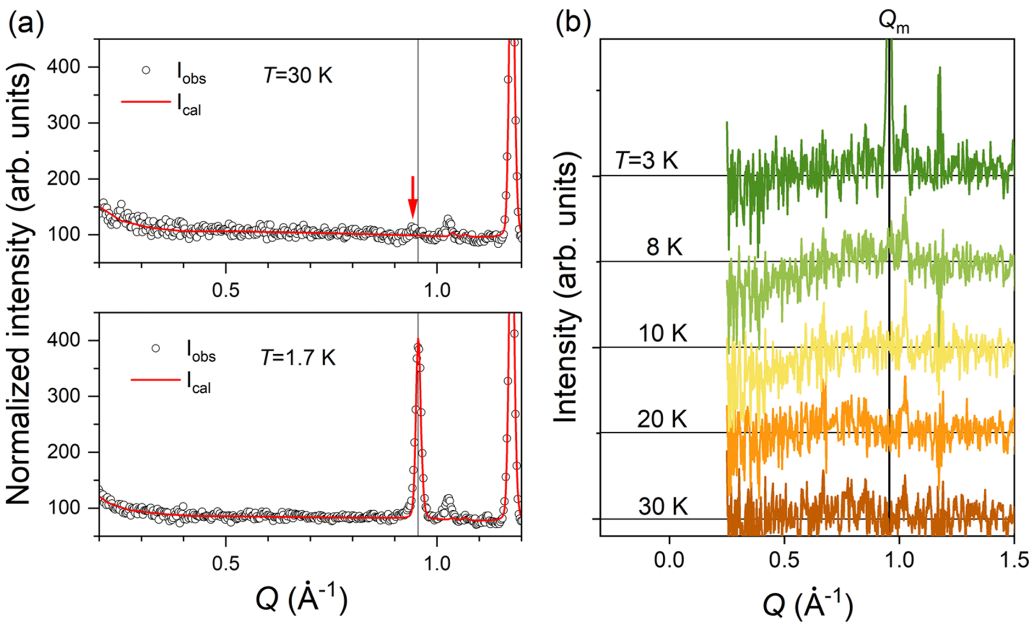

FIG. 10. (a) Low-Q region of the neutron powder diffraction for $Ba_2FeSi_2O_7$ at 1.7 and 30 K. Red arrow and solid black line indicate the remaining peak at 30 K and magnetic Bragg peak position, $Q_m = (1,0,1/2) \sim 0.95$ Å^{-1}, respectively. (b) Subtraction of the 50 K data from the low-temperature data. Horizontal solid black lines indicate the offset of each data.

strong easy-planar magnetic anisotropy, providing a suitable playground to test intriguing physics of the low dimensional quantum magnetism.

ACKNOWLEDGMENTS

We thank V. S. Zapf, C. D. Batista, H. Zhang, J.-H. Choi, and D. Bahng for useful discussions and C. Won for crystal growth. This work was supported by the Max Planck POSTECH/Korea Research Initiative, Study for Nano Scale Optomaterials and Complex Phase Materials (Grant No. 2016K1A4A4A01922028) and Grant No. 2020M3H4A2084418, through the National Research Foundation (NRF) funded by MSIP of Korea. Neutron diffraction and data analysis performed by S.-H. D. and A.D.C. were supported by the U.S. DOE, Office of Science, Basic Energy Sciences, Materials Sciences and Engineering Division. M.L. acknowledges the National High Magnetic Field Laboratory in-house science program funded by the National Science Foundation through cooperative Grant No. DMR 1157490, the State of Florida, and the U.S. Department of Energy. We acknowledge the support of the National Institute of Standards and Technology, U.S. Department of Commerce, in providing the neutron research facilities used in this work. The work at Rutgers University was supported by the U.S. DOE under Grant No. DOE: DE-FG02-07ER46382.

APPENDIX A: X-RAY DIFFRACTION DATA FOR CRUSHED SINGLE CRYSTALS

Figure 9 shows the XRD pattern for crushed single crystals of $Ba_2FeSi_2O_7$ at $T = 300$ K. The refined crystallographic parameters are tabulated in Table III. The XRD patterns confirms the single phase $Ba_2FeSi_2O_7$ but also exhibits that there exist preferred crystallographic orientations.

APPENDIX B: NEUTRON POWDER DIFFRACTION DATA AT DIFFERENT TEMPERATURES

Figure 10 presents the low-Q diffraction data measured at several temperatures, to show that the small peak remaining at 20 and 30 K is most likely a small impurity peak. In Fig. 10(a), the small peak shown at 30 K (red arrow) slightly mismatches the magnetic Bragg peak at $Q_m = (1,0,1/2) \sim 0.95$ Å^{-1} (solid black line). To subtract the higher temperature data provides further clarity, Fig. 10(b) presents the subtraction of the 50 K data from the lower temperature data. In this subtracted data, the small peak is consistently absent at all temperatures. This result indicates that the peak is temperature independent across a broad temperature range, including T_N, and hence most likely arises from a small impurity phase in the sample.

[1] N. D. Mermin and H. Wagner, Phys. Rev. Lett. **17**, 1133 (1966).

[2] A. Orendáčová, R. Tarasenko, T. Vladimír, E. Čižmár, M. Orendáč, and A. Fehe, Crystals **9**, 6 (2019).

[3] L. Onsager, Phys. Rev. **65**, 117 (1944).

[4] A. Cuccoli, T. Roscilde, V. Tognetti, R. Vaia, and P. Verrucchi, Phys. Rev. B **67**, 104414 (2003).

[5] Y. Kohama, M. Jaime, O. E. Ayala-Valenzuela, R. D. McDonald, E. D. Mun, J. F. Corbey, and J. L. Manson, Phys. Rev. B **84**, 184402 (2011).

[6] J. M. Kosterlitz and D. J. Thouless, J. Phys. C: Solid State Phys. **6**, 1181 (1973).
[7] A. Cuccoli, T. Roscilde, R. Vaia, and P. Verrucchi, Phys. Rev. B **68**, 060402(R) (2003).
[8] N. Tsyrulin, F. Xiao, A. Schneidewind, P. Link, H. M. Rønnow, J. Gavilano, C. P. Landee, M. M. Turnbull, and M. Kenzelmann, Phys. Rev. B **81**, 134409 (2010).
[9] P. Sengupta, C. D. Batista, R. D. McDonald, S. Cox, J. Singleton, L. Huang, T. P. Papageorgiou, O. Ignatchik, T. Herrmannsdörfer, J. L. Manson, J. A. Schlueter, K. A. Funk, and J. Wosnitza, Phys. Rev. B **79**, 060409(R) (2009).
[10] E. Čižmár, S. A. Zvyagin, R. Beyer, M. Uhlarz, M. Ozerov, Y. Skourski, J. L. Manson, J. A. Schlueter, and J. Wosnitza, Phys. Rev. B **81**, 064422 (2010).
[11] P. Sengupta, A. W. Sandvik, and R. R. P. Singh, Phys. Rev. B **68**, 094423 (2003).
[12] C. Yasuda, S. Todo, K. Hukushima, F. Alet, M. Keller, M. Troyer, and H. Takayama, Phys. Rev. Lett. **94**, 217201 (2005).
[13] H. Murakawa, Y. Onose, S. Miyahara, N. Furukawa, and Y. Tokura, Phys. Rev. Lett. **105**, 137202 (2010).
[14] I. Kézsmárki, N. Kida, H. Murakawa, S. Bordács, Y. Onose, and Y. Tokura, Phys. Rev. Lett. **106**, 057403 (2011).
[15] S. Bordács, I. Kézsmárki, D. Szaller, N. Kida, H. Murakawa, Y. Onose, R. Shimano, T. Rõõm, U. Nagel, S. Miyahara, N. Furukawa, and Y. Tokura, Nat. Phys. **8**, 734 (2012).
[16] K. Penc, J. Romhányi, T. Rõõm, U. Nagel, A. Antal, T. Fehér, A. Jánossy, H. Engelkamp, H. Murakawa, Y. Tokura, D. Szaller, S. Bordács, and I. Kézsmárki, Phys. Rev. Lett. **108**, 257203 (2012).
[17] M. Soda, L.-J. Chang, M. Matsumoto, V. O. Garlea, B. Roessli, J. S. White, H. Kawano-Furukawa, and T. Masuda, Phys. Rev. B **97**, 214437 (2018).
[18] P. Barone, K. Yamauchi, and S. Picozzi, Phys. Rev. B **92**, 014116 (2015).
[19] T. T. Mai, C. Svoboda, M. T. Warren, T.-H. Jang, J. Brangham, Y. H. Jeong, S.-W. Cheong, and R. Valdés Aguilar, Phys. Rev. B **94**, 224416 (2016).
[20] W. Low and M. Weger, Phys. Rev. **118**, 1119 (1960).
[21] D. Dai, H. Xiang, and M.-H. Whangbo, J. Comput. Chem. **29**, 2187 (2008).
[22] S.-H. Do, H. Zhang, T. J. Williams, T. Hong, V. O. Garlea, J. A. Rodriguez-Rivera, T.-H. Jang, S.-W. Cheong, J.-H. Park, C. D. Batista, and A. D. Christianson, Nat. Commun. **12**, 5331 (2021).
[23] B. E. Warren, Z. Kristallogr. **74**, 131 (1930).
[24] V. Hutanu, A. Sazonov, H. Murakawa, Y. Tokura, B. Náfrádi, and D. Chernyshov, Phys. Rev. B **84**, 212101 (2011).
[25] M. Soda, M. Matsumoto, M. Månsson, S. Ohira-Kawamura, K. Nakajima, R. Shiina, and T. Masuda, Phys. Rev. Lett. **112**, 127205 (2014).
[26] J. Rodríguez-Carvajal, Physica B **192**, 55 (1993).
[27] A. S. Wills, Physica B **276–278**, 680 (2000).
[28] C. Kittel, *Introduction to Solid State Physics* (Wiley, New York, 1995).
[29] E. Gamsjager and M. Wiessner, Monatsh. Chem. **149**, 357 (2018).
[30] Z. Zhang, K. Wierschem, I. Yap, Y. Kato, C. D. Batista, and P. Sengupta, Phys. Rev. B **87**, 174405 (2013).
[31] M. Matsumoto, M. Soda, and T. Masuda, J. Phys. Soc. Jpn. **82**, 093703 (2013).
[32] M. Matsumoto, J. Phys. Soc. Jpn. **83**, 084704 (2014).
[33] A. Jain, M. Krautloher, J. Porras, G. H. Ryu, D. P. Chen, D. L. Abernathy, J. T. Park, A. Ivanov, J. Chaloupka, G. Khaliullin, B. Keimer, and B. J. Kim, Nat. Phys. **13**, 633 (2017).
[34] S.-M. Souliou, J. Chaloupka, G. Khaliullin, G. Ryu, A. Jain, B. J. Kim, M. Le Tacon, and B. Keimer, Phys. Rev. Lett. **119**, 067201 (2017).